Journal of Alloys and Compounds 666 (2016) 108–117

Contents lists available at ScienceDirect

Journal of Alloys and Compounds

journal homepage: http://www.elsevier.com/locate/jalcom

A pathway to optimize the properties of magnetocaloric $Mn_{2-x}Fe_xP_{1-y}Ge_y$ for magnetic refrigeration

D.M. Liu [a, b, *], Z.L. Zhang [a], S.L. Zhou [b], Q.Z. Huang [c], X.J. Deng [a], M. Yue [b], C.X. Liu [a], J.X. Zhang [b], J.W. Lynn [c]

[a] Beijing Key Lab of Microstructure and Property of Advanced Material, Institute of Microstructure and Property of Advanced Materials, Beijing University of Technology, Beijing, 100124, China
[b] Key Laboratory of Advanced Functional Materials, Education Ministry of China, Beijing University of Technology, Beijing, 100124, China
[c] NIST Center for Neutron Research, National Institute of Standards and Technology, Gaithersburg, MD, 20899, USA

ARTICLE INFO

Article history:
Received 16 October 2015
Received in revised form
7 January 2016
Accepted 8 January 2016
Available online 11 January 2016

Keywords:
Magnetocaloric effect
MnFePGe compound
First-order transition
Neutron diffraction

ABSTRACT

Magnetocaloric materials can be useful in magnetic refrigeration applications, but to be practical the magneto-refrigerant needs to have a very large magnetocaloric effect (MCE) near room temperature for modest applied fields (<2 T) with small hysteresis and magnetostriction, and should have a complete magnetic transition, and environmentally friendly. One system that may fulfill these requirements is $Mn_{2-x}Fe_xP_{1-y}Ge_y$, where a combined first-order structural and magnetic transition occurs between the high temperature paramagnetic and low temperature ferromagnetic phase. We have used neutron diffraction, differential scanning calorimetry, and magnetization measurements to study the effects of Mn and Ge location in the structure on the ordered magnetic moment, MCE, and hysteresis for a series of compositions of the system near optimal doping. The diffraction results indicate that the Mn ions located on the 3*f* site enhance the desirable properties, while those located on the 3 g sites are detrimental. The phase fraction that transforms, hysteresis of the transition, and entropy change can be affected greatly by both the compositional homogeneity and the particle size, and an annealing procedure has been developed that substantially improves the performance of all three properties of the material. We also establish a correlation between applied magnetic field to complete the transition and the temperature range of coexistence of the PM and FM phase. On the basis of these results we have identified a pathway to understand the nature and to optimize the MCE properties of this system for magnetic refrigeration applications.

1. Introduction

Magnetic refrigeration based on the magnetocaloric effect (MCE) has attracted recent interest as a potential replacement for the classical vapor compression systems in use today, especially for the use at room temperature (RT) [1–5]. For a transition that is purely magnetic in origin, which is typically a second order (continuous) in nature, the MCE is insufficiently high to improve the refrigeration efficiency. To increase the entropy change at the phase transition, systems with concomitant magnetic and structural transitions, which are first order (discontinuous), can greatly increase the MCE, but at the cost of hysteresis and transitions that are phase-incomplete. To be considered for practical application at room temperature in magnetocaloric refrigeration the first-order transition must have: (i) a large entropy change ΔS associated with the transition from a disordered to a ordered magnetic structure; (ii) a transition occurring near room temperature, (iii) a small hysteresis ΔT_{hys}; (iv) a low applied magnetic field ΔB to induce the transition; v) a small temperature/applied magnetic field range of coexistence of the ordered and disordered phases; (vi) and a complete magnetic transition, i.e. there should be no, or very small, residual untransformed material when the process is completed.

The choice of the materials studied so far has been made mainly on the basis of the magnitude of the entropy change. Some examples of materials with the giant magnetocaloric effect with transitions near room temperature are $Gd_5Si_2Ge_2$ [6],

* Corresponding author. Institute of Microstructure and Property of Advanced Materials, Beijing University of Technology, Beijing, 100124, China.
E-mail address: dmliu@bjut.edu.cn (D.M. Liu).

http://dx.doi.org/10.1016/j.jallcom.2016.01.074
0925-8388/

$MnFeP_{0.45}As_{0.55}$ [7], $LaFe_{13-x}Si_x$ [8], MnAs [9], $(La_{0.8-y}Ca_{0.2})MnO_3$ for $0.03 \leq y \leq 0.1$ [10], and Ni_2MnGa [11]. In addition, for low temperature magnetic refrigeration rare earth based intermetallic compounds such as TmCuAl [12], the RT_2X_2 series like $NdMn_{2-x}Ti_xSi_2(0 \leq x \leq 0.3)$ [13], $HfFe_6Ge_6$-type intermetallics like $YMn_6Sn_{6-x}Ti_x$ [14], can be important. All of these materials undergo a first-order transition at T_C, and display some common properties such as hysteresis, particle size effects, and coexistence of the two phases near T_C. Typically detailed crystallographic studies of the structures as a function of temperature and magnetic field have not been undertaken, including the temperature/applied field range of coexistence of the two phases, particle size and about the completeness of the transition. We have found that such crystallographic details can provide important information about the systems and how to optimize their properties.

The $Mn_{2-x}Fe_xP_{1-y}Ge_y$ material is one such system with a combined structural and magnetic transition from the paramagnetic (PM) to ferromagnetic (FM) state. Compared with the pure metal Gd, it has a large entropy change; besides it has no use of expensive or toxic elements such as Gd in $Gd_5(Si_xGe_{1-x})_4$ and As in $Mn_{2-x}Fe_xP_{1-y}As_y$ [15–17]. Trung et al. [18] reported a comprehensive study for a variety of compositions in the $Mn_{2-x}Fe_xP_{1-y}Ge_y$ system and found that the thermal hysteresis can be tunable. They also showed that the value of the Curie temperature (T_C) increases when the Ge content increases and decreases when the Mn content increases. Leitão et al. reported [19] that the T_C of the Fe rich side of the $(Mn,Fe)_2(P,Ge)$ system is easy to tune with careful manipulation of Fe and Ge content, but the ferro–paramagnetic transition sharpness is adversely affected. In our previous work [20–23] the crystal and magnetic structures for the compound with composition $Mn_{1.1}Fe_{0.9}P_{0.8}Ge_{0.2}$ and $Mn_{1.1}Fe_{0.9}P_{0.76}Ge_{0.24}$ were determined by neutron powder diffraction (NPD), while the crystal structure for $Mn_{1.2}Fe_{0.9}P_{0.76}Ge_{0.24}$ was determined by XRD [24]. These compounds have the Fe_2P-type structure (space group $P\,\bar{6}\,2m$) and undergo a combined first-order structural and magnetic transition from a paramagnetic to a ferromagnetic phase. In those studies we found that the two phases coexist in an interval of applied magnetic-field/temperature, and that the range of coexistence depends on the composition. In general, the transition does not go to completion so that there is a remnant untransformed fraction of material. In this paper we investigate this problem in $Mn_{2-x}Fe_xP_{1-y}Ge_y$ for a number of compositions, with the goal of elucidating in detail the effects of composition, particle size, method of preparation, and crystal structure on the physical properties, so that the correlation between the composition and physical properties can be established, and an optimized composition identified. The results also can be used to help understand the nature of the physical properties of other first-order transition materials.

2. Experimental

$Mn_{2-x}Fe_xP_{1-y}Ge_y$ (x = 0.8, 0.9; y = 0.2, 0.22, 0.24) powders were prepared by ball milling. Polycrystalline samples were subsequently obtained by the spark plasma sintering method as described in previous work [25]. Detailed temperature and magnetic field neutron diffraction measurements were carried out on the high-intensity BT9 triple axis spectrometer at the NIST Center for Neutron Research (NCNR) using pyrolytic graphite monochromator and filter, with a wavelength of 2.359 Å. Neutron powder diffraction data were also collected on the high resolution powder neutron diffractometer (BT1), with monochromatic neutrons of wavelength 1.5403 Å produced by a Cu(311) monochromator. We remark that for neutron diffraction the Fe and Mn scattering amplitudes have opposite signs making them very easy to distinguish. NPD measurements were carried out as a function of both magnetic field and temperature employing a vertical field 7 T superconducting magnet.

The temperature and field dependences of the bulk magnetization were measured with a Quantum Design superconducting quantum interference (SQUID) instrument. The temperature steps were 1 K closer to the transition and 2 K further away. A Netzsch differential scanning calorimetry 204 F1 was used for calorimetric measurements. The sample of about 30 mg was investigated by heating at the rates of 1 K/min and 5 K/min.

Temperature-dependent x-ray diffraction measurements were carried out with a Bruker D8 Advance equipment. Scanning Electron Microscopy (SEM) data were obtained using a FEI Quanta 250, and Electron Backscatter Diffraction (EBSD) measurements using an EDAX/TSL system were used to investigate the microstructure. Energy-dispersive X-ray spectroscopy (EDAX) and scanning transmission synchrotron radiation X-ray microscope experiments were used for elemental distribution analysis.

3. Results and discussion

3.1. Crystal and magnetic structures

The crystal and the magnetic structures of $Mn_{2-x}Fe_xP_{1-y}Ge_y$ are shown in Fig. 1. $Mn_{2-x}Fe_xP_{1-y}Ge_y$ adopts the hexagonal Fe_2P-type structure with partial substitution of Mn for Fe and Ge for P [20]. The crystal structures of the $Mn_{2-x}Fe_xP_{1-y}Ge_y$ samples were refined in the hexagonal space group $P\bar{6}2m$ with the GSAS program [26] using neutron powder diffraction data collected at 295 K. Nominal and refined compositions are given in Table 1, where we note that the refined Mn compositions are slightly less than the nominal ones while the Fe content is slightly higher, it may due to that Mn is easy to be evaporated at high temperature in the process of preparation. In the structure of $Mn_{2-x}Fe_xP_{1-y}Ge_y$ for $x < 1$, most or all the Mn atoms are located in the 3*g* (*x*,0,1/2) sites. When $x > 1$, most or all the Mn atoms in excess of 1 occupy the 3*f* (*x*,0,0) sites and will be indicated as % of Mn at 3*f* with the symbol *n*%Mn at 3*f*, where *n* is the site occupancy factor of Mn. It is found that *n*%Mn at 3*f* has a corresponding relation with some important magnetocaloric properties as discussed below. The substitution of Mn for Fe atoms in the 3*f* site (*n*%Mn at 3*f*) is also provided in Table 1. Note that the *n* % Mn at 3*f* depends on the Mn/Fe ratio. Substitution of Ge for P leads to a random distribution of Ge in each of the 1*b* and 2*c* sites, with the Ge preferentially locating in the 2*c* sites.

Three typical samples with nominal compositions $Mn_{1.2}Fe_{0.8}P_{0.76}Ge_{0.24}$ (sample #1), $Mn_{1.1}Fe_{0.9}P_{0.76}Ge_{0.24}$ (samples #2), and $Mn_{1.1}Fe_{0.9}P_{0.8}Ge_{0.2}$ (samples #3) have been selected to carry out detailed temperature and magnetic field dependent neutron diffraction measurements. Structural parameters of these samples are given in Table 2. Some data for #2 and #3 have been reported in previous works [20] and [23], in this paper we use them for comparing and discussion. The refined compositions for these

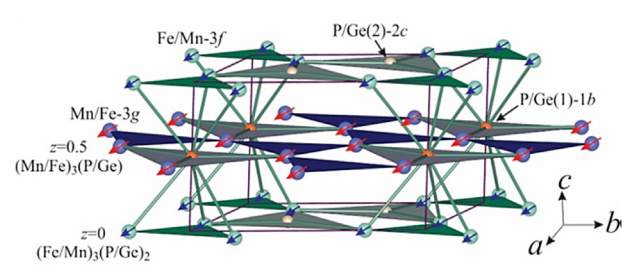

Fig. 1. Crystal and magnetic structure of $Mn_xFe_{2-x}P_{1-y}Ge_y$.

Table 1
Nominal and refined compositions, substitution of Mn for Fe atoms in the 3*f* site (*n*% Mn at 3*f*) of the samples. Refined compositions were obtained by NPD on the sintered bulk samples.

Sample	Nominal composition	Refined composition	*n*%Mn at 3*f* (295K)
LZ091- 1#	$Mn_{1.2}Fe_{0.8}P_{0.76}Ge_{0.24}$	$Mn_{1.17}Fe_{0.83}P_{0.74}Ge_{0.26}$	17.03
LZ092	$Mn_{1.2}Fe_{0.8}P_{0.76}Ge_{0.24}$	$Mn_{1.17}Fe_{0.83}P_{0.74}Ge_{0.26}$	17.4
LZ094	$Mn_{1.2}Fe_{0.8}P_{0.76}Ge_{0.24}$	$Mn_{1.16}Fe_{0.84}P_{0.76}Ge_{0.24}$	16.4
LL083	$Mn_{1.1}Fe_{0.9}P_{0.76}Ge_{0.24}$	$Mn_{1.06}Fe_{0.94}P_{0.80}Ge_{0.20}$	6.7
LL084- 2#	$Mn_{1.1}Fe_{0.9}P_{0.76}Ge_{0.24}$	$Mn_{1.05}Fe_{0.95}P_{0.83}Ge_{0.17}$	7.7
YM04	$Mn_{1.1}Fe_{0.9}P_{0.76}Ge_{0.24}$	$Mn_{1.05}Fe_{0.95}P_{0.80}Ge_{0.20}$	6
YM01- 3#	$Mn_{1.1}Fe_{0.9}P_{0.8}Ge_{0.2}$	$Mn_{1.06}Fe_{0.94}P_{0.76}Ge_{0.24}$	6.2
YM05	$Mn_{1.1}Fe_{0.9}P_{0.8}Ge_{0.2}$	$Mn_{1.06}Fe_{0.94}P_{0.82}Ge_{0.18}$	6.8
YM06	$Mn_{1.1}Fe_{0.9}P_{0.8}Ge_{0.2}$	$Mn_{1.05}Fe_{0.95}P_{0.78}Ge_{0.22}$	6.8
YMA11	$Mn_{1.1}Fe_{0.9}P_{0.8}Ge_{0.2}$	$Mn_{1.06}Fe_{0.94}P_{0.76}Ge_{0.24}$	6.2
YM02	$Mn_{1.1}Fe_{0.9}P_{0.78}Ge_{0.22}$	$Mn_{1.06}Fe_{0.94}P_{0.77}Ge_{0.23}$	7.2

three samples as indicated in Table 1 can be written as #1-Mn($Fe_{0.83}Mn_{0.17}$) ($P_{0.74}Ge_{0.26}$), #2-($Mn_{0.973}Fe_{0.027}$) ($Fe_{0.923}Mn_{0.077}$) ($P_{0.83}Ge_{0.17}$) and #3-($Mn_{0.994}Fe_{0.006}$) ($Fe_{0.938}Mn_{0.062}$) ($P_{0.76}Ge_{0.24}$), where we have explicitly indicated the Mn content on the two different sites.

3.2. Temperature and field induced transition

Thermomagnetic curves *M-T* have been measured for the three samples and are shown in Fig. 2a, and are compared in Fig. 2b with the FM phase fractions as a function of temperature (*Frac*(FM)-*T*) derived from monitoring the integrated intensities of the (001) neutron Bragg reflection upon warming and cooling. Note that the *c*-axis lattice parameters in the paramagnetic and ferromagnetic phases are quite different, so that the $(001)_{PM}$ and $(001)_{FM}$ reflections are easily distinguishable with NPD [20,21]. The ferromagnetic transition temperature (T_C), thermal hysteresis (ΔT_{hys}), and the temperature range of coexistence of the PM and FM phases (ΔT_{coex}) [20,21] are given in the figures and are quite different for the three samples. For each sample, the corresponding values of T_C derived from the *M-T* and *Frac*(FM)-*T* curves are in good agreement on both warming and cooling. The values of ΔT_{hys} and ΔT_{coex} observed in the neutron experiments are larger than those derived in the magnetization measurements, which we attribute to the much larger NPD sample size (10 g versus 0.1 g) and the hysteresis of the temperature controller for neutron measurements. The neutron data (Fig. 2b) show that over this temperature range only ~85% of the PM phase (PMP) is transformed into the FM phase (FMP) in all three samples. The remaining PM phase slowly transformed to FM phase continually as the temperature was further decreased. But quite a little of PM phase, however, still existed at the lowest temperature we measured. In this work, we use the temperature or magnetic field dependent NPD or XRD measurements to obtain the FM phase fraction during the FM-PM transition, using the following formula:

$$\mathrm{FMP\%} = \frac{I_{\mathrm{FMP}}}{I_{\mathrm{FMP}} + I_{\mathrm{PMP}}} \tag{1}$$

In order to explore the effects of an applied magnetic field on the PM-FM transition, neutron diffraction data were collected under fields of 0–7 T. As an example, data obtained from sample #1 are shown in Fig. 3a, in which the integrated intensity of the (001) reflection of the PM phase is plotted as a function of the magnetic field at different temperatures near T_C. The data indicate that the PM-FM transition takes place above a critical field B_{on} which is defined as the field where the transition just starts to occur, and it can be seen that B_{on} depends on the measured temperature. The same as B_{on}, the field B_{end} is defined as the field accesses to the completion (*end*) of the transition, when the field goes beyond B_{end} the transition becomes dramatically slow. Both B_{on} and B_{end} were determined at different temperatures by neutron diffraction for a variety of $Mn_{2-x}Fe_xP_{1-y}Ge_y$ samples listed in Table 1. These data were used to construct the magnetic phase diagram shown in the inset of Fig. 3a. Between B_{on} and B_{end}, the PM and FM phases coexist and the range of coexistence is about 1T. The B_{on} and B_{end} curves are almost parallel and increase approximately linearly with increasing temperature at the rate dB_{on}/dT of about 0.3T/K. This indicates that the temperature dependence of B_{on} is strong, which is a favorable property for obtaining high values of ΔS_M due to the fact that according to the Clausius–Clapeyron relation [27] the magnetic entropy change depends not only on the magnetization jump at T_C but also on the temperature dependence of B_{on}. For all the other samples we obtained B_{end} at T_C, so that ΔB is almost equal to B_{end}.

To clearly illustrate the tendency of the transition from PM to FM, we plot the FM phase fraction as a function of magnetic field for temperature of 262.5K in Fig. 3b. The trends of the transition at all of the temperatures in Fig. 3a are similar, the data at 262.5K was choice was an example. Of course B_{on} and B_{end} at 262.5K are higher than those at 261K. The remaining PM continues to transform slowly at higher magnetic fields. Note that only about 87% of the PM phase is transformed into the FM phase at 4T, in agreement with the results of the temperature-induced PM-FM transition shown in

Table 2
Structural parameters of $Mn_{2-x}Fe_xP_{1-y}Ge_y$. The ferromagnetic structure has magnetic symmetry *P11m′* with moments for Mn and Fe that lie within the *a-b* plane. For convenience in the refinements the moment was set parallel to the *a* direction; the moment direction within the *a-b* plane cannot be determined by NPD.

Sample	#1, $x = 1.17$, $y = 0.26$	#2, $x = 1.05$, $y = 0.17$	#3, $x = 1.06$, $y = 0.24$
MnO impurity [%]	3.4(2)	4.5(1)	3.4(2)
PMP fraction [%]	96.6(2)	95.5(1)	96.6(2)
c/a of PM at 295 K	0.56482(1)	0.56964(1)	0.57088(1)
c/a of FM after T-PFT, 0 T	0.54568(4), at 250K 0.5502, at 262 K	0.54544(2), at 259K	0.54384(2), at 230K
c/a of FM after F-PFT	0.54714(4), 262K/3T	0.54673(2),271K/3T	0.54600(2), 253K/5T
$\Delta(c/a)$ (*T*) in T-PFT, 0 T	0.0191(1), 295K–250K 0.0146(1), 295 K–262K	0.0242(1), 295k ~259K	0.0270(1), 295k ~230K
$\Delta(c/a)$ (*B*) in F-PFT	0.0177(1), 295K -262K/0-3T	0.0229(1), 295K -271K/0-3T	0.0249(1), 295K -253K/0-5T
M_{Fe} (*T*) [μ_B] (in T-PFT), 0 T	0.35(7), at 250K	0.73(6), at 259 K	1.14(9), at 230 K
M_{Mn} (*T*) [μ_B] (inT-PFT), 0 T	3.15(7), at 250K	3.56(5), at 259 K	3.57(9), at 230 K
$M_{f.u}$(*T*) [μ_B](in T-PFT), 0 T	3.50(10), at 250K	4.30(8), at 259 K	4.7(1), at 230 K
M_{Fe} (*B*) [μ_B] (in F-PFT)	0.89(9), 262K/0-3T	0.75(8), 271K/0-3T	0.80(7), 253K/0-5T
M_{Mn} (*B*) [μ_B] (in F-PFT)	3.70(9), 262K/0-3T	3.91(8), 271K/0-3T	4.49(8), 253K/0-5T
$M_{f.u}$ (*B*) [μ_B] (in F-PFT)	4.59(10), 262K/0-3T 4.30(1), 262K/0-1T	4.64(10), 271K/0-3T 4.72(10), 271K/0-6T	5.5(1), 253K/0-3T 5.6(1), 253K/0-5T

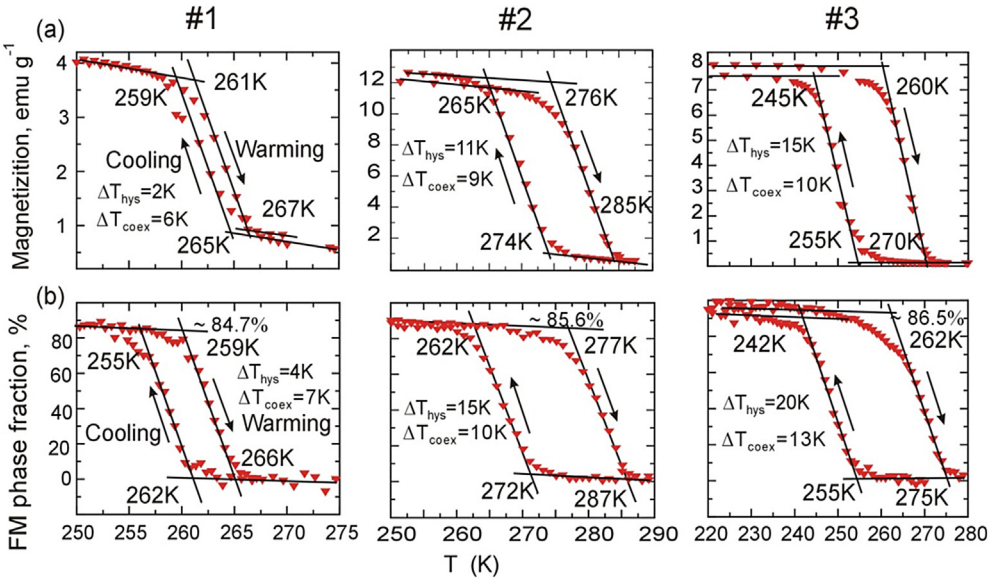

Fig. 2. (a) Temperature dependence of the magnetization *M-T* of $Mn_xFe_{2-x}P_{1-y}Ge_y$ for three polycrystalline compositions (see Table 1) obtained on warming and cooling under an external magnetic field of 0.05 T. Note that 1 emu/g = 1 Am^2/kg; (b) FM phase fraction as a function of temperature upon warming and cooling under zero applied field.

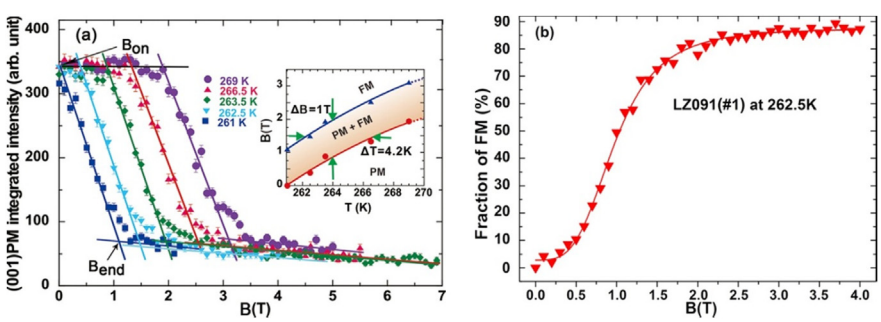

Fig. 3. (a) $(001)_{PM}$ integrated intensity of sample #1 as a function of magnetic field at different temperatures. Inset: magnetic phase diagram for sample #1 obtained from neutron data. (b) FM phase fraction as a function of magnetic field.

Fig. 2b. Our NPD results show that this untransformed PM phase is of existence at all the measured temperature, and as we will demonstrate below originates from the fraction of particles that have a small size.

For practical applications it is necessary to complete the PM-FM transition at a low enough field so that current permanent magnetic technology can be employed, and highly desirable to be low enough to use inexpensive magnets. Fig. 4 demonstrates that there is direct correlation between ΔT_{coex} and B_{end}, *i.e.*, the larger is ΔT_{coex}, the larger is B_{end}. The data were collected from the eleven sintered samples listed in Table 1. For each sample, we determined the value of B_{end} as displayed in Fig. 3a and derived ΔT_{coex} from the differential scanning calorimetry (DSC) results as indicated in Fig. 5a. Of course ΔT_{coex} can also been obtained by neutron or X-ray diffraction methods as shown in Fig. 2b, but DSC results are more accurate and the way is easy to be carried on. It has been shown that the coexistence of the PM and FM phases in the temperature interval ΔT_{coex} is partly due to the inhomogeneity of the distribution of component atoms in the structure [31,32]. It follows, therefore, that the system will have small values of B_{end} when the chemical inhomogeneity is reduced or eliminated by means of appropriate preparation and treatment of the samples.

3.3. Relationships between n%Mn at 3f site and physical properties

The PM and FM phases in all the compounds have the same crystal symmetry ($P\bar{6}2m$) and structure, and therefore we expect that the observed variations of the physical properties must be strongly correlated with the chemical composition and the distribution of the atoms in the structure. In this paper the

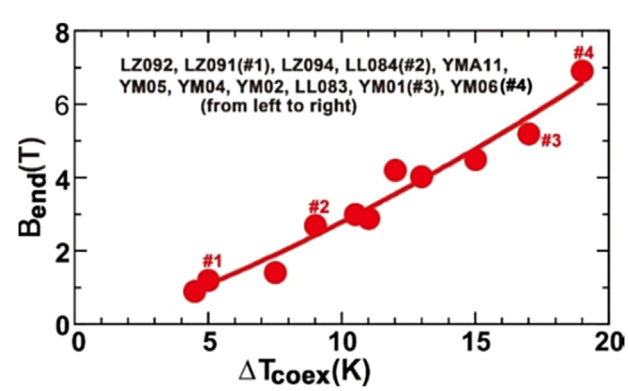

Fig. 4. Plot of B_{end} as a function of ΔT_{coex}.

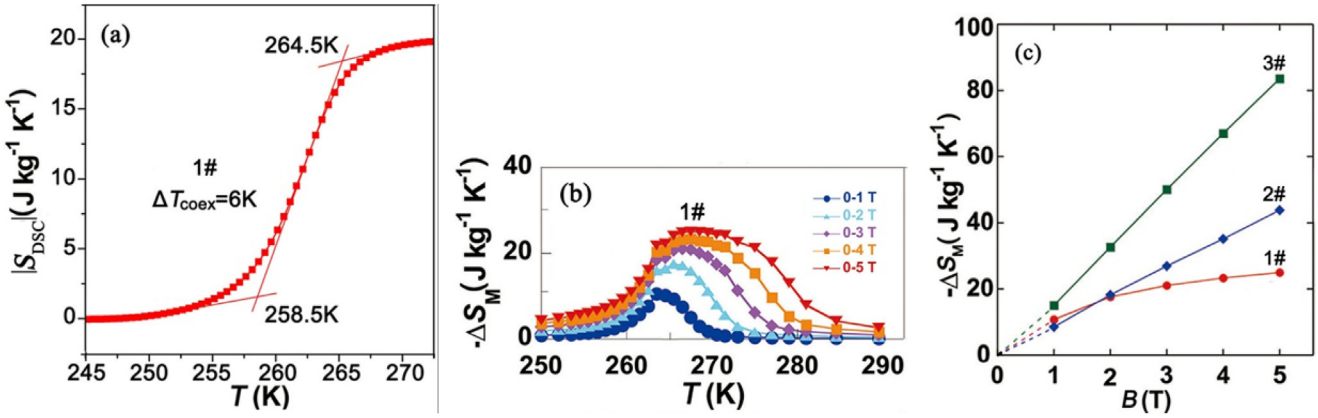

Fig. 5. a) Zero field entropy changes as a function of temperature obtained from DSC data taken with 5 K/min for sample #1; b) Temperature dependence of the magnetic entropy change of sample #1 as a function of applied magnetic field determined using the Maxwell relation. c) The peak $-\Delta S_M$ as a function of external magnetic field at T_C for the three $Mn_xFe_{2-x}P_{1-y}Ge_y$ samples.

magnetocaloric properties of all samples were determined from calorimetric and magnetic measurements and used for the following discussion.

Typically the MCE is derived from magnetic measurements with the use of the Maxwell relation, but the reliability of this procedure in the case of first order transitions is controversial [28,29]. Therefore, for our system, calorimetric measurements with a DSC have been made to obtain the latent heat and the entropy change directly, which can then be compared with the magnetic measurements [22]. In the present alloy system, the strongly first order transition occurs from a paramagnetic (PM) to a ferromagnetic (FM) phase and can be induced either by temperature or by an applied magnetic field. Our investigations indicate that the two processes exhibit essentially identical evolutions regarding the crystal and magnetic structures, indicating they should have the similar entropy change. We therefore conclude that the ΔS obtained by the DSC method (where the transition is temperature induced) is valid also for this magnetically induced transition, thus avoiding uncertainties connected with the magnetic measurements [22].

The total entropy of the transition was evaluated by numerical integration of the expression

$$\Delta S_{DSC} = S_{T2} - S_{T1} = \int_{T1}^{T2} C_P \frac{dT}{T} \tag{2}$$

where C_P is the zero-field heat capacity.

Fig. 5a shows ΔS_{DSC} of obtained from the DSC data for sample 1# as a function of temperature at rates of 5 K/min on warming. In the experiments we found that different rate of temperature change had no significant effect on ΔS [22]. The transition temperatures almost agree with the results obtained from the *M-T* data and from the neutron measurements (Fig. 2). The entropy changes ΔS_{DSC} directly measured were corrected for the effect of the incompleteness of the PM-FM transition and for the small MnO impurity content, to obtain results assuming metallurgically ideal samples [30].

In this work the magnetic entropy change ΔS_M for the eleven samples as a function of temperature and for different magnetic fields were also evaluated by the same method as the references [6–11]. Determination of the isothermal ΔS_M from *M-B* data is commonly done using the Maxwell equation $\Delta S_M = S_M(T,B) - S_M(T,0) = \int_0^B (\partial M/\partial T)dB$. According to the reference [33], ΔS_M can be obtained by field sweep, temperature sweep or magnetization, in the present work what we used is magnetization. In Fig. 5b we show the curves $-\Delta S_M$ for sample 1# as a function of temperature and for different magnetic fields. The calculated maximum are $|\Delta S_M| = 25.1$, 43.8, and 83.5 J kg^{-1}K^{-1} for samples #1, #2, and #3 at $\Delta B = 5$T, respectively. When normalized assuming ideal properties, these values increase to 29.6, 51.2, and 96.5 J kg^{-1} K^{-1}. The $|\Delta S_M|$ for #3 was reported in Fig. 1b in Ref. [20] and for #2 was reported in Ref. [22]. In this study we re-measured $|\Delta S_M|$ for sample #3 and used it for comparing with other samples. Here, we need to emphasize that although the Maxwell relation is controversial as mentioned above but the values of $|\Delta S_M|$ calculated by the same method are still comparable.

Fig. 5c shows the peak $-\Delta S_M$ as a function of external applied field at T_C. For samples #2 and #3, $|\Delta S_M|$ increases linearly with increasing field at a rate of 9.7, and 20.2 J kg^{-1}K^{-1}T^{-1}, respectively, while for sample #1 the rate is 8.4 J kg^{-1}K^{-1}T^{-1} below 2 T, and only 1.4 J kg^{-1}K^{-1}T^{-1} above 2 T. Since the completing field for the transition is 1.2 T, as mentioned above in Fig. 3a, this behavior indicates that $-\Delta S_M$ of sample #1 is nearly saturated at ~1.2 T at T_C. The values of $-\Delta S_M$ for #2 and #3 continue increasing with field up to more than 5 T, indicating that these transitions are not complete until high fields are applied.

Tables 2 and 3 give the structural parameters and magnetic properties of the three $Mn_{2-x}Fe_xP_{1-y}Ge_y$ samples, 1#, 2# and 3#. Fig. 6 shows some of the data for all eleven compounds, where the normalized $^*\Delta S_{DSC}$ were obtained from ΔS_{DSC}:

$$^*\Delta S_{DSC} = \frac{\Delta S_{DSC}}{FM\% \times (1 - Impurity\%)} \tag{3}$$

Indeed the data reported in Table 3 and Fig. 6 show that the substitution of Mn for Fe atoms at 3*f* site (*n*%Mn at 3*f*) plays a very important role in this system. More specifically, when *n*%Mn at 3*f* increases from 6.2% in sample #3–17% in sample #1, the magnetic moments decrease from 4.7 to 3.5 μ_B for $M_{f.u.}(T)$ and from 5.5 to 4.59 μ_B for $M_{f.u.}(B)$, with a consequent decrease in the normalized $-^*\Delta S_{DSC}$ from 48.4 to 35.5 J kg^{-1} K^{-1} (Table 3 and Fig. 6a). Most importantly, there is a huge decrease of the thermal hysteresis ΔT_{hys} from 15 to 2 K, and a huge decrease of the magnetic field saturation requirement B_{end} from 5.2 to 1.2 T (Table 3 and Fig. 6d. Fig. 6c shows that the ratios of $-^*\Delta S_{DSC}/M_{f.u.}(T)$, $\Delta(c/a)/M_{f.u.}(T)$, and $-^*\Delta S_{DSC}/\Delta c/a$ *vs.* *n*%Mn at 3*f* are almost constant, and that the ratio $-^*\Delta S_{DSC}/M_{f.u.}(T)$ has a constant value of about 10 J kg^{-1} K$^{-1}\mu_B^{-1}$ for the three samples. This behavior suggests that the total entropy change and the magnetostriction effect are linearly correlated with

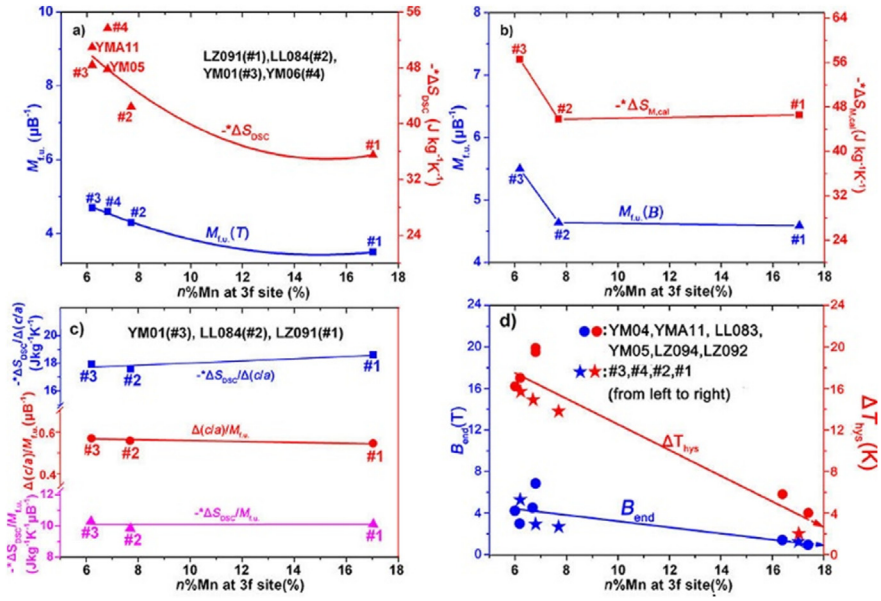

Fig. 6. Variation of some physical properties of the compounds of the system $Mn_{2-x}Fe_xP_{1-y}Ge_y$ as a function of the atomic per cent of Mn in the 3f position of space group $P\bar{6}2m$: a) total magnetic moments $M_{f.u.}(T)$, $M_{Mn}(T)+M_{Fe}(T)$ of the FM phase, obtained from the temperature dependent NPD, and $-{}^*\Delta S_{DSC}$ normalized and calculated (The 'normalized' entropy change is obtained by scaling the measured ΔS_{DSC} by assuming a 100% conversion of PM to FM); b) total magnetic moments $M_{f.u.}(B)$, $M_{Mn}(B)+M_{Fe}(B)$, of the FM phase, obtained with an applied magnetic field of 1 and 3T from NPD measurements. The 'calculated' ${}^*\Delta S$ is obtained by ${}^*\Delta S_{M,cal} = M_{f.u.}(B){}^*\Delta S_{DSC}/M_{f.u.}(T)$; c) this figure shows that the changes of $-{}^*\Delta S_{DSC}$ and $\Delta(c/a)$ as a function of n% are related by the equation ${}^*\Delta S_{DSC} = k \times \Delta(c/a)$ where k is a constant. Similar behavior is found for ${}^*\Delta S_{DSC}$ and the total magnetic moment $M_{f.u.}(T)$ (see also Fig. 7). It follows that $\Delta(c/a)/M_{f.u.}(T) = k'/k$ where $-{}^*\Delta S_{DSC}/M_{f.u.}(T) = k'$. The ratio k'/k is slightly sloping down as n% increases; d) the values of B_{end} (magnetic field value at the end of the transition) and ΔT_{hys} as function of n%. Note that ΔT_{hys} decreases sharply as n% increases. The B_{end} for the sample LZ092 is as small as 0.9T, but is 7T for YM05.

Table 3
Magnetic properties of $Mn_{2-x}Fe_xP_{1-y}Ge_y$.

Sample	#1, $x = 1.17$, $y = 0.26$	#2, $x = 1.05$, $y = 0.17$	#3, $x = 1.06$, $y = 0.24$
$-{}^a\Delta S_{DSC}$ J $Kg^{-1}K^{-1}$, 0 T	35.5	42.4	48.4
$-{}^{**}\Delta S_{M,\ calc}$ J $kg^{-1}K^{-1}$	46.6 (3T), 43.6 (1 T)	45.8 (3T), 46.5 (6T)	56.6 (3T), 57.7 (5T)
T_C (K)	267	285	270
ΔT_{hys} (K)	2	11	15
ΔT_{coex} (K)/B_{end} (T)	6/1.2	9/2.7	17/5.2
FMP fraction (%)	84.7 at 250 K	85.6 at 259 K	86.5 at 230 K

[a] Here we adjust the measured entropy ΔS_{DSC} via $\Delta S_{M,\ calc} = M_{f.u.}(B) \times [\Delta S_{DSC}/M_{f.u.}(T)]$ with the ordered magnetic moments determined by the NPD measurements to reflect the magnetic entropy.

the ordered magnetic moment. The function $-{}^*\Delta S_{DSC}$ *vs.* $M_{f.u.}(T)$ is also plotted in the lower part of Fig. 7. The upper part of the figure shows that $-\Delta S_M$, evaluated using the equation $\Delta S_M^{max} = R\ln(2J+1)$ [34] *vs.* the moment is also almost linear in the range between 2 and 6 μ_B. On the basis of these results, a compound like sample #1 with ~19% Mnat 3*f* is expected to have a large MCE $-(-\Delta S_{M,calc}$ in Table 3), between 35 and 46 J kg^{-1} K^{-1}, with small hysteresis (ΔT_{hys} close to 0 K) and a required magnetic field to complete the transition of less than 1.2 T Fig. 6d.

From Table 1 we find that the *n*%Mn at 3*f* value depends on the Mn/Fe ratio but not on the Ge/P ratio in the alloys. As the concentration of Mn atoms located in the 3f sites changes, the parameters corresponding to the most important physical properties are significantly affected, as shown in Table 3 and Fig. 6. (We note that in discussing the values of ΔS_{DSC}, the direct calorimetric measurements made with a DSC will be used rather than the values obtained with the Maxwell relation using the magnetization curves).

In order to have a large MCE with a low applied magnetic field, the material must have a sharp first-order transition with a large entropy change from one state to the other, and large ordered magnetic moments. It is also important to have a small thermal hysteresis to reduce losses, and a small magnetostriction for mechanical stability. The hysteresis will in fact reduce the

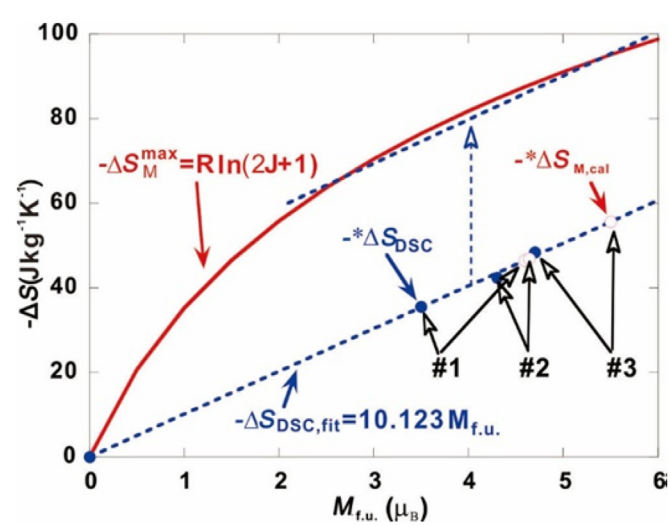

Fig. 7. Plot of $-\Delta S_M^{max}$, $-{}^*\Delta S_{DSC}$ and $-{}^*\Delta S_{M\ calc}$ *vs.* the total magnetic moment $M_{f.u.}(T)$. ${}^*\Delta S_{M\ calc}$ was calculated with the equation ${}^*\Delta S_{M\ calc} = M_{f.u.}(B) \times [{}^*\Delta S_{DSC}/M_{f.u.}(T)]$. Note that it is almost linear in the range between 2 μ_B and 6μ_B.

magnetocaloric working efficiency. However, for sample #1, the reduction of $M_{f.u.}(T)$ can be circumvented by using an applied magnetic field of 1.2 T, with a consequent change of the moment from 3.5 to 4.3 μ_B and a corresponding increase of MCE from 35.5 to 43.6 J kg^{-1} K^{-1}. The small hysteresis for sample #1 can be attributed to the large substitution of Mn for Fe at the 3f site and that of Ge for P. This is because 1) the larger the substitution, the easier chemical homogeneity can be obtained. and 2) the Ge substitution for P increases T_C while Mn substitution for Fe decreases T_C, and as a consequence there is little change of T_C [17,18] in every crystallite particle in the sample. Thus, the magnetic field required for the PM-FM transition is reduced.

The study of a number of samples with different compositions (Table 3 and Fig. 6) has shown that when *n*%Mn at 3*f* increases, a decrease is observed of the following parameters associated with the transition: (i) total magnetic moment ($M_{f.u.} = M_{Mn} + M_{Fe}$); (ii) entropy change $^*\Delta S$; (iii) hysteresis $\Delta T_{hys.}$; (iv) value of the applied magnetic field at the end of transition B_{end}; (v) magnetostriction $\Delta(c/a)$; (vi) critical temperature T_C. Some of these variations are desirable (e.g. hysteresis, B_{end}, $\Delta(c/a)$, T_C) others are not (e.g. magnetic moment, entropy change), and, therefore, compromises will have to be made to obtain a compound suitable for practical applications. Fig. 6c shows that the variation of $-^*\Delta S_{DSC}$ and of $\Delta(c/a)$ as a function of *n*%Mn at 3*f* is related by the equation $-^*\Delta S_{DSC} = k \times \Delta(c/a)$, where k is constant. Similar behavior is found for $-^*\Delta S_{DSC}$ and the total magnetic moment $M_{f.u.}(T)$. (see Fig. 6). It therefore follows that $\Delta(c/a)/M_{f.u.}(T) = k'/k$, where $k' = -^*\Delta S_{DSC}/M_{f.u.}(T)$. (in fact k'/k is very slightly sloping down as *n*% Mn at 3*f* increases). Two of the most important properties that a magnetocaloric material must have to be a candidate for technological applications are a small hysteresis of the PM to FM transitions and a small magnetic field necessary to induce the transition around room temperature. As shown in Fig. 6d, both properties are strongly dependent on *n*% Mn at 3*f*, making the Mn content of a compound of the $Mn_{2-x}Fe_xP_{1-y}Ge_y$ system one of the primary factors in optimizing the properties for practical applications.

3.4. Effects of crystallite size and inhomogeneities of composition on the transition

As shown in Figs. 2b and 3, the PM-FM transition is not complete, and it has been observed that the diffraction lines of the residual PM phase are considerably broadened, indicating the small size of the PM crystallites that don't transform.

Fig. 8 shows the magnetization curves of the powder (YMP20) and SPS synthesis (YM01) samples of $Mn_{1.1}Fe_{0.9}P_{0.8}Ge_{0.2}$ as a function of temperature. The YMP20 sample was prepared by ball milling while the YM01 sample was prepared by spark plasma sintering. A ferromagnetic transition occurs near 250 K for the YM01 sample but no sharp transformation was observed in the measurement for the YMP20 powder. The inset shows that the primary difference between the two sample is that the width of the 001 PM and FM reflections is much larger in the case of YMP20 (at 15 K) than that of YM01 (at 245 K). Correspondingly, the magnetization curve of YM01 is sharp, and that of YMP20 remains practically unchanged between 4 and 300 K. This indicates that the small sizes of the crystallites (estimated from the width of the (001) Bragg peaks to be about 50 nm for YMP20) inhibit the transition. These results demonstrate that the particle size plays an essential role in the magnetocaloric properties.

Fig. 9a,b display the zero-field temperature dependence of the intensities and widths of the 001 PM and FM peaks for the YM01 $Mn_{1.1}Fe_{0.9}P_{0.8}Ge_{0.2}$ sintered sample, collected on warming at 10 K/hour. The inset shows the diffraction scan (2θ) of the 001 PM and FM peaks at the indicated temperatures. At 200 K, a fraction of the

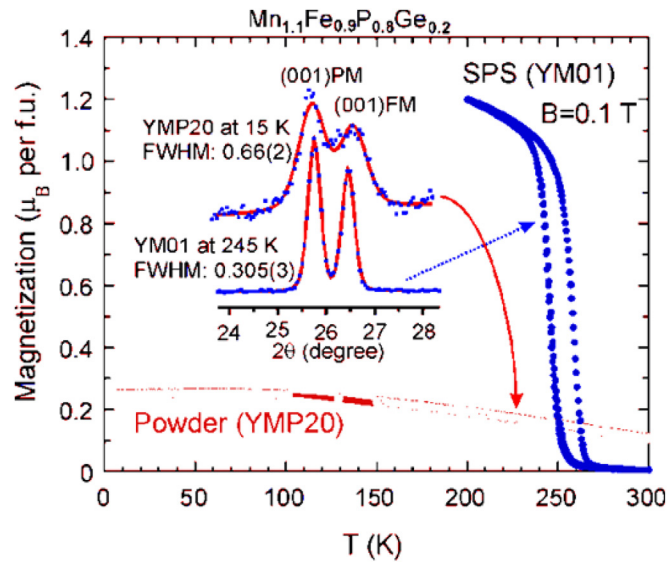

Fig. 8. Magnetization vs temperature plots of the Ball Milled and Spark Plasma Sintering (SPS) samples (YMP20 and YM01[Figure 4a in reference 20], respectively) obtained from the compound having nominal composition $Mn_{1.1}Fe_{0.9}P_{0.8}Ge_{0.2}$. The neutron diffraction profiles of the (001)PM and (001)FM reflections produced by the two samples are shown in the inset. The results demonstrate that in the case of YMP20 (very broadened peaks) the transition from PM to FM is hindered because the crystallites are too small to allow the ordering of the magnetic moments, while in the case of YM01 (sharp peaks) the transition occurs as expected.

sample is still in the PM phase, and clearly consists of very small crystallites, as indicated by the large width of the 001 PM peak. The contribution of the small crystallites to the width of the 001 PM peak begins to be significant at 265 K and keeps increasing down to 200 K. Note that the width of the FM peak is constant over the entire range of temperatures. The phase transition occurs in the interval 258–275 K ($\Delta T = 17$ K), in which the intensity changes with a steep slope, and, at a much slower rate, in the interval 248–258 K. The slope in the range 258–275 K indicates inhomogeneities of composition, and the small departures from linearity are due to the fact that the compositional variations in the sample are not quite uniform.

Fig. 9c,d display the magnetic field dependence of the intensities and widths of the 001 PM and FM peaks for the YM01 $Mn_{1.1}Fe_{0.9}P_{0.8}Ge_{0.2}$ sintered sample at 255 K, the PM-FM Curie temperature T_C. Between 0 and 2.6 T the intensities of the two peaks vary slowly, between 2.6 T and 5.5 T the variation is more pronounced, and finally between 5.5 T and 6.9 T the remaining PM phase essentially does not convert into FM. Interestingly, the FWHM of (001) PM increases in this last interval significantly, confirming once again that the smallest crystallites in the sample are responsible for the incompleteness of the transformation.

A comparison of Fig. 9c with Fig. 9a indicates that the effect of an applied magnetic field is similar to that produced by lowering the temperature, as it should be, since both induce the ferromagnetic ordering of the spins of the magnetic atoms. The two methods, however, are not identical, as the changes of intensity and FWHM of the (001) PM reflections are not as well defined in the case of the applied field. One reason for this behavior is that the moments prefer to lie in-plane, while the applied field in a powder makes all angles with respect to the easy plane. Conversely, when lowering the temperature the internally generated in-plane field assists the external field in facilitating the PM to FM transition. This suggests that developing sample preparation techniques that produced preferred orientation of the material should further improve the

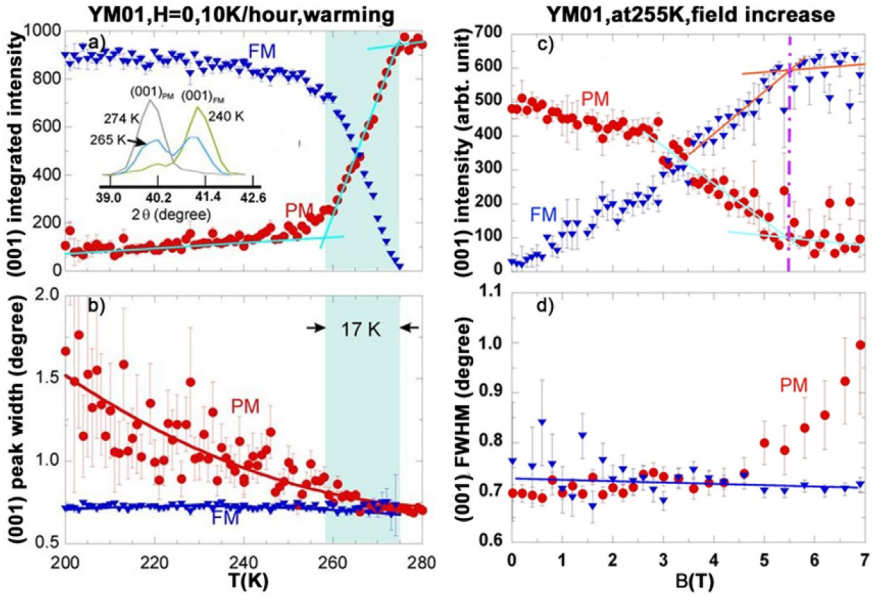

Fig. 9. Neutron diffraction intensities of the (001) PM and FM reflections as a function of: a) temperature and c) applied magnetic field for the YM01 sample. The corresponding line widths are shown in b) and d), respectively. The figure illustrates that in both the temperature and magnetic field induced transitions: (i) the transition is not complete, (ii) the ranges of coexistence of the two phases are large and, (iii) the broadening of both the FM and PM peaks at the beginning and at the end of the transition is quite evident. As explained in the text, these features are due to the distribution of crystallite sizes in the sample. The inset shows the profiles of the (001) Bragg peak in the PM and FM phases at three temperatures.

MCE performance.

It is clear that the size of the crystallites plays an important role in the fraction of the sample that transforms, as the data in Fig. 9 demonstrate that the largest crystallites transform first, leaving the smaller crystallites in the PM phase; hence the broadened Bragg peak. In addition, we know from previous work that compositional variations affect both the transition temperature and phase fraction that converts [20–22]. We have therefore undertaken additional characterization and annealing studies in order to unravel these two contributions to the performance of the material and to establish a procedure to improve the performance.

The distribution of compositions in these $Mn_{2-x}Fe_xP_{1-y}Ge_y$ alloys was investigated by SEM + EDAX and scanning transmission synchrotron radiation X-ray microscope experiments. The latter X-ray measurements were carried out at the Shanghai Synchrotron Radiation Facility [35], which provided chemical mapping with a spatial resolution of 30 nm. Mn, Fe and Ge were chosen to be scanned separately at the absorption edge and then distributions of these elements were obtained. The element mappings do not show significant inhomogeneity.

SEM + EDAX analysis shows that in our $Mn_{2-x}Fe_xP_{1-y}Ge_y$ alloys, Ge readily accumulates at grain boundaries. Fig. 10a shows the backscattered electron SEM image of the DMD01 $Mn_{1.2}Fe_{0.8}P_{0.76}Ge_{0.24}$ bulk sample. The white lines located at the grain boundaries were analyzed by EDAX which indicated that those are areas with enhanced Ge content.

In order to ascertain the effects of both particle size and inhomogeneities on the magnetocaloric properties, subsequent homogenizing treatments were applied to the sample DMD01 with compositions $Mn_{1.2}Fe_{0.8}P_{0.76}Ge_{0.24}$. The heat treatments were performed by annealing at 950 °C for 15 h, followed by at 850 °C for 48 h. The annealed sample was renamed as DMD02. After such heat treatments, the compositional homogeneity improved and the grains increased in size, substantially improving the

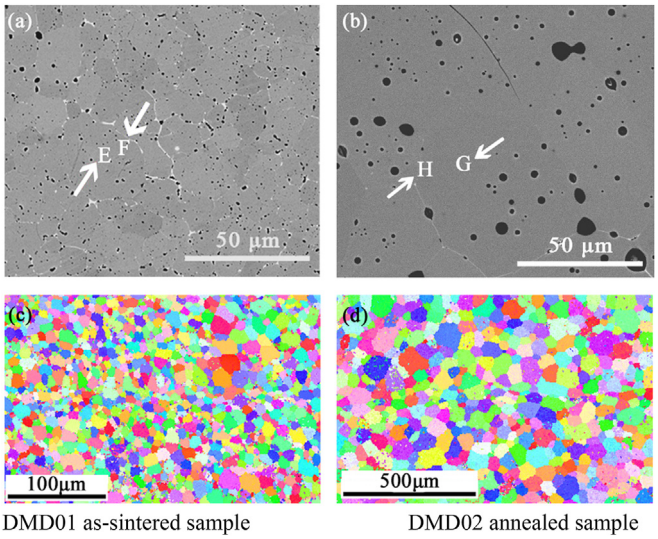

Fig. 10. Backscattered scanning electron microscopy (SEM-BSE) images (a, b) and electron back scattered diffraction (EBSD) images (c, d) of the compound $Mn_{1.2}Fe_{0.8}P_{0.76}Ge_{0.24}$ for a, c) the initial sintered, and b, d) post-annealed samples. The white lines in a) indicate grain boundaries that are rich in Ge. The arrows indicate the points where the SEM-BSE analysis was performed (E and G in-grain points, and F and H grain-boundary points). The black spots in (a, b) are holes. The different shades (colors) appearing in the EBSD images (c, d) are due to the different orientations of the crystallites. Lower magnification was used during the EBSD measurements for statistical purposes. (For interpretation of the references to colour in this figure legend, the reader is referred to the web version of this article.)

Table 4
Atomic distributions of the DMD01 as-sintered and DMD02 annealed $Mn_{1.2}Fe_{0.8}P_{0.76}Ge_{0.24}$ sample.

	Mn	Fe	P	Ge
E, in grain, DMD01	1.2096	0.7903	0.7837	0.2291
F, grain boundary, DMD01	1.0978	0.9463	0.5296	1.1296
G, in grain, DMD02	1.2061	0.8015	0.7874	0.2323
H, grain boundary, DMD02	1.2043	0.7982	0.7786	0.2758

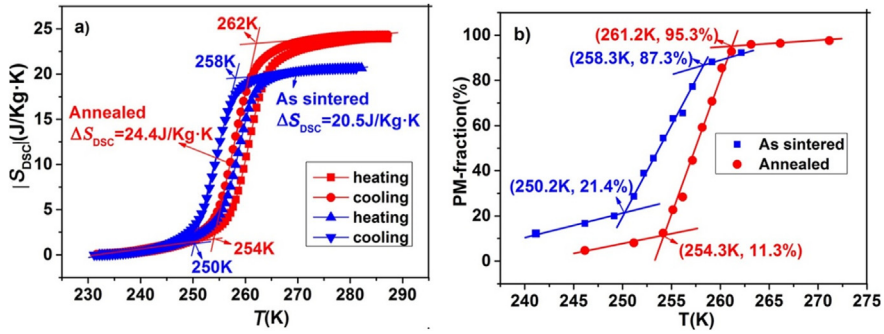

Fig. 11. (a) $|S_{DSC}|$*vs* temperature plots. The (blue) triangles represent the behavior of the DMD01 sample (as sintered) and the (red) square/circles that of DMD02 (annealed). The increase in the value of ΔS for the annealed sample is due to the increase of the FM phase fraction in DMD02. (b) Phase fraction for the sintered [(blue) squares] and annealed [(red) circles] samples vs. temperature. (For interpretation of the references to colour in this figure legend, the reader is referred to the web version of this article.)

magnetocaloric properties as we now discuss.

Fig. 10b shows the SEM image of the DMD02 $Mn_{1.2}Fe_{0.8}P_{0.76}Ge_{0.24}$ sample, comparing it to the sample before annealing (Fig. 10a). Note that the Ge concentration at the grain boundaries obviously has been reduced. Table 4 gives the atomic distributions at four points (E, F, G, H) calculated from the EDAX analysis. Note in particular that the data at F indicate that the grain boundaries in the DM01 sample are rich in Ge and poor in P. Most importantly, after the annealing procedure we find that the grain size has increased dramatically as indicated in Fig. 10b,d for the annealed sample, with the average grain size increasing from 10 to 50 μm.

Fig. 11 presents the $|S_{DSC}|$-T curves, and the temperature dependence of the content of the paramagnetic phase percentage calculated from X-ray diffraction for the as-sintered and annealed $Mn_{1.2}Fe_{0.8}P_{0.76}Ge_{0.24}$ alloys. The transition range ΔT of the DMD01 and DMD02 samples is 8.1 K and 6.9 K, respectively, while the residual PM phase at the end temperatures of the transition is 21% and 11.8%. Our previous study demonstrated that the magnetic-entropy change directly corresponds to the phase fraction of the magnetic transition [20]. Fig. 11a shows that the ΔS_{DSC} values for DMD01 and DMD02 are 20.5 J/kg K and 24.4 J/kg K, respectively, while the thermal hysteresis of DMD02 was reduced from 3.8 K to 3.4 K. Thus the magnetocaloric properties are substantially improved in all aspects by the above annealing procedures.

4. Conclusions

The magnetocaloric properties of the $Mn_{2-x}Fe_xP_{1-y}Ge_y$ system near optimal doping have been investigated in detail using a variety of experimental techniques to determine the crystallographic structure, caloric behavior, and morphology of the system. We find that compositional homogeneity and particle size play an essential role in optimizing the MCE properties, and an annealing procedure has been developed to optimize these properties. Neutron diffraction, differential scanning calorimetry, and magnetization measurements, have been used to determine the effects of the Mn content and crystallographic location, and of Ge content, on the crystal structure, the magnetic moment, the magnetic entropy change, hysteresis, and saturation field of the first-order PM-FM combined magnetic and structural transition in the $Mn_{2-x}Fe_xP_{1-y}Ge_y$ system. The results show that when n%Mn at 3f increases from 6.2% to 17%, the magnetic moments decrease from 4.7 to 3.41 μ_B for the temperature induced moment $M_{f.u.}(T)$, and from 5.5 to 4.59 μ_B for the magnetic field induced moment, $M_{f.u.}(B)$, with a consequent decrease of the entropy change $^*\Delta S_{DSC}$ (measured by DSC) from 48.4 to 35.5 J kg^{-1} K^{-1}. At the same time, however, the hysteresis decreases dramatically from 15 K to 2 K, and the value of the applied magnetic field required to complete the PM-FM transition near T_C decreases radically from 7 T to 0.9 T. Thus the important properties of these materials can be tuned by composition and preparation methods to provide to optimize those properties relevant for refrigerant applications. There is an important correlation between applied magnetic field to complete the transition and the temperature range of coexistence of the PM and FM phase. We believe that these conclusions should also apply to other compounds with the Fe_2P-type structure.

Acknowledgments

The authors are grateful to Anthony Santoro for valuable discussions and the BL08U Beam line of the Shanghai Synchrotron Radiation Facility (SSRF) for the synchrotron radiation X-ray measurements. This work supported in part by the Natural Science Foundation of Beijing (KZ201410005005) and the Research Fund for the Doctoral Program of Higher Education of China (20121103110028). The identification any commercial products does not imply endorsement or recommendation by the National Institute of Standards and Technology.

References

[1] J. Glanz, Science 279 (1998) 2045.
[2] M.H. Phan, S.C. Yu, J. Magn. Magn. Mater 308 (2007) 325.
[3] K.A. Gschneidner Jr., V.K. Pecharsky, Int. J. Refrig. 31 (2008) 945.
[4] A. Smith, C.R.H. Bahl, R. Bjørk, K. Engelbrecht, K.K. Nielsen, N. Pryds, Adv. Energy Mater 2 (2012) 1288.
[5] L. Mañosa, A. Planes, M. Acet, J. Mater. Chem. A 1 (2013) 4925.
[6] K.V. Pecharsky, K.A. Gschneidner, Phys. Rev. Lett. 78 (1997) 4494.
[7] O. Tegus, E. Brück, K.H.J. Buschow, F.R. de Boer, Nature 415 (2002) 150.
[8] F.X. Hu, B.G. Shen, J.R. Sun, Z.H. Cheng, G.H. Rao, X.X. Zhang, Appl. Phys. Lett. 78 (2001) 3675.
[9] H. Wada, Y. Tanabe, Appl. Phys. Lett. 79 (2001) 3302.
[10] W. Chen, W. Zhong, C.F. Pan, H. Chang, Y.W. Du, Acta Phys. Sin. 50 (2001) 319.
[11] M. Pasquale, C.P. Sasso, L.H. Lewis, J. Appl. Phys. 95 (2004) 6918.
[12] Z.J. Mo, J. Shen, L.Q. Yan, J.F. Wu, L.C. Wang, J. Lin, C.C. Tang, B.G. Shen, Appl. Phys. Lett. 102 (2013) 192407.
[13] M.F. Md Din, J.L. Wang, S.J. Campbell, R. Zeng, W.D. Hutchison, M. Avdeev, S.J. Kennedy, S.X. Doum, J. Phys. D. Appl. Phys. 46 (2013) 445002.
[14] S.Y. Zhang, P. Zhao, R.W. Li, H.W. Zhang, B.G. Shen, J. Appl. Phys. 91 (2002) 5250.
[15] W. Dagula, O. Tegus, X.W. Li, L. Song, E. Brück, D.T. Cam Thanh, F.R. de Boer, K.H.J. Buschow, J. Appl. Phys. 99 (2006) 105.
[16] D.T. Cam Thanh, E. Brück, O. Tegus, J.C.P. Klaasse, T.J. Gortenmulder, K.H.J. Buschow, J. Appl. Phys. 99 (2006) 08Q107.
[17] Z.Q. Ou, G.F. Wang, L. Song, O. Tegus, E. Brück, K.H.J. Buschow, J. Phys. Condens. Matter 18 (2006) 11577.
[18] N.T. Trung, Z.Q. Ou, T.J. Gortenmulder, O. Tegus, K.H.J. Buschow, Appl. Phys. Lett. 94 (2009) 102513.
[19] J.V. Leitão, M. van der Haar, A. Lefering, E. Brück, J. Magn. Magn. Mater 344 (2013) 49.
[20] D.M. Liu, M. Yue, J.X. Zhang, T.M. McQueen, W.J. Lynn, X.L. Wang, Y. Chen, J. Li, R.J. Cava, X. Liu, Z. Altounian, Q. Huang, Phys. Rev. B 79 (2009) 014435.

[21] D.M. Liu, Q.Z. Huang, M. Yue, W.J. Lynn, L.J. Liu, Y. Chen, Z.H. Wu, J.X. Zhang, Phys. Rev. B 80 (2009) 174415.
[22] M. Yue, D.M. Liu, Q.Z. Huang, T. Wang, F.X. Hu, J.B. Li, G.H. Rao, B.G. Shen, J.W. Lynn, J.X. Zhang, J. Appl. Phys. 113 (2013) 043925.
[23] L.J. Liu, D.M. Liu, Q.Z. Huang, T.L. Zhang, L. Zhang, M. Yue, W.J. Lynn, J.X. Zhang, Powder Diffr. 3 (2010) 25.
[24] H. Xu, M. Yue, C. Zhao, D.T. Zang, J.X. Zhang, Rare Met. 31 (2012) 336.
[25] M. Yue, Z.Q. Li, X.L. Wang, D.M. Liu, J.X. Zhang, X.B. Liu, J. Appl. Phys. 105 (2009) 07A915.
[26] A. Larson, R.B. Von Dreele, GSAS: Generalized Structure Analysis System, 1994.
[27] A. Giguère, M. Foldeaki, B. Ravi Gopal, R. Chahine, T.K. Bose, A. Frydman, J.A. Barclay, Phys. Rev. Lett. 83 (1999) 2262.
[28] J.D. Zou, B.G. Shen, B. Gao, J. Shen, J.R. Sun, Adv. Mater 21 (2009) 693.
[29] G.J. Liu, S.J.R. un, J. Shen, B. Gao, H.W. Zhang, F.X. Hu, B.G. Shen, Appl. Phys. Lett. 90 (2007) 032507.
[30] D.M. Liu, H. Zhang, S.B. Wang, W.Q. Xiao, Z.L. Zhang, N. Tian, C.X. Liu, M. Yue, Q.Z. Huang, J.X. Zhang, J.W. Lynn, J. Alloys Comp. 633 (2015) 120–126.
[31] C.R.H. Bahl, R. Bjørk, A. Smith, K.K. Nielsen, J. Magn. Magn. Mate 324 (2012) 564.
[32] J.S. Amaral, P.B. Tavares, M.S. Reis, J.P. Araujo, T.M. Mendonca, V.S. Amaral, J.M. Vieira, J. Non-Cryst. Solids 354 (2008) 5301.
[33] J.C.B. Monteiro, R.D. dos Reis, A.M. Mansanares, F.G. Gandra, Appl. Phys. Lett. 105 (2014) 074104.
[34] A.M. Tishin, Y.I. Spichkin, Institute of Physics, Bristol and Philadelphia, first ed., vol. 1, 2003, p. 351. Chap. 11.
[35] C.F. Xue, Y. Wang, Z. Guo, Y.Q. Wu, X.J. Zhen, M. Chen, J.H. Chen, S. Xue, Z.Q. Peng, Q.P. Lu, R.Z. Tai, Rev. Sci. Instr. 81 (2010) 103502.